Electronic supplementary information for

A Chemopalette Strategy for White Light by Modulating Monomeric and Excimeric Phosphorescence of a Simple Cu(I) Cyclic Trinuclear Unit

Hu Yang,‡[ab] Ji Zheng,‡[a] Su-Kao Peng,[a] Xiao-Wei Zhu,[a] Meng-Yan Wan,[a] Weigang Lu[a] and Dan Li[*,a]

[a]College of Chemistry and Materials Science, Jinan University, Guangzhou 510632, P. R. China.
[b]Department of Chemistry, Shantou University, Guangdong 515063, P. R. China.
‡ Hu Yang and Ji Zheng contributed equally to this work

Table of Contents

Experimental Section

Materials. Chemicals and solvents were purchased and used as received without further purification.

Methods. UV-Vis absorption spectra were recorded on a Bio-Logic MOS-500 multifunctional circular dichroism spectrometer. Infrared spectra were obtained in KBr disks on a Thermo Scientific FTIR Nicolet is10 spectrometer in the range of 4000~400 cm^{-1}, and abbreviations used for the IR bands are: w = weak, m = medium, b = broad, s = strong, vs = very strong. Elemental analyses were carried out with an Elementar vario MICRO CUBE equipment. Powder X-ray diffraction (PXRD) experiments were performed on an Rigaku Ultima IV X-ray diffractometer (Cu Kα, λ = 1.5418 Å) in the step of 0.02° under the conditions 40 KV and 40 mA. Steady state photoluminescence spectra were recorded by a single-photon counting spectrometer on a Flourolog Horiba spectrofluorometer at room temperature. PTI Quanta Master Model QM/TM scanning spectrofluorometer recorded the variable temperature solid-state emission spectra. Absolute quantum yield was recorded by Hamamatsu C11347-01 absolute PL quantum yield spectrometer under room temperature. The different concentrations of **Cl-α** were achieved by adding different amounts of samples into KBr for solid-state emission measurements. Thermogravimetric analysis curve was recorded by TGA Q50 V20.6 with a heating rate of 10 °C/min from 40 to 800 °C in a N_2 atmosphere.

Synthesis and characterization

Cl-α

Cu(NO$_3$)$_2$·3H$_2$O (60.4 mg) and 4-chloropyrazole (51.26 mg) were dissolved in ethanol, then diluted with ethanol into 25.00 mL, so that the concentration of the Cu^{2+} ion and 4-chloropyrazolate are 0.01 mol/L and 0.02 mol/L, respectively. 2.00 ml of above solution was added into a clean and heavy-wall glass tube, followed by the addition of 1.00 mL of chlorobenzene. After flame sealed, these tubes were heated at 140 °C in an oven for 12 h and cooled to room temperature at a rate of 5 °C/h. The yield is 83.3% for **Cl-α** based on Cu(NO$_3$)$_2$·3H$_2$O.

Cl-β

Cu(NO$_3$)$_2$•3H$_2$O (241.60 mg) and 4-chloropyrazole (102.52 mg) were dissolved in ethanol, then diluted with ethanol into 100 mL, so that the concentration of the Cu^{2+} ion and 4-chloropyrazolate are 0.01 mol/L and 0.01 mol/L, respectively. 2.00 mL of above solution was added into a clean and dry heavy-wall glass tube, followed by the addition of 1.00 mL of chlorobenzene. After flame sealed, these tubes were heated at 140 ℃ in an oven for 24 h and cooled to room temperature at a rate of 5 ℃/h. Colorless needle crystals were collected and air-dried, although sometimes mixed with **Cl-α**, suggested by their different emission colors (blue for **Cl-α** and orange for **Cl-β**) under 365 nm UV light. The yield is 54.5% for **Cl-β** based on Cu(NO$_3$)$_2$•3H$_2$O.

FT-IR and Elemental analyses

Cl-α

FT-IR (KBr pellet, cm^{-1}): 3122(m), 1643(m), 1392(s), 1302(s), 1223(w), 1197(s), 1160(s), 1054(s), 1012(m), 970(s), 832(s), 613(s). Elemental analyses (Cu$_3$C$_9$H$_6$N$_6$Cl$_3$), calculated (%): C 21.83, H 1.22, N 16.97; found (%): C 22.25, H 1.28, N 16.56.

Cl-β

FT-IR (KBr pellet, cm^{-1}): 3118(m), 1644(m), 1388(s), 1298(s), 1223(w), 1198(s), 1157(s), 1056(s), 1010(w), 968(s), 833(s), 820(s), 611(s). Elemental analyses (Cu$_3$C$_9$H$_6$N$_6$Cl$_3$), calculated (%): C 21.83, H 1.22, N 16.97; found (%): C 22.05, H 1.31, N 16.59.

Caution! In the solvothermal crystallization processes, the volume of solution should not exceed one third of the volume of the glass tubes. Be careful and avoid potential empyrosis and incised wound when flame-sealing and opening the glass tubes.
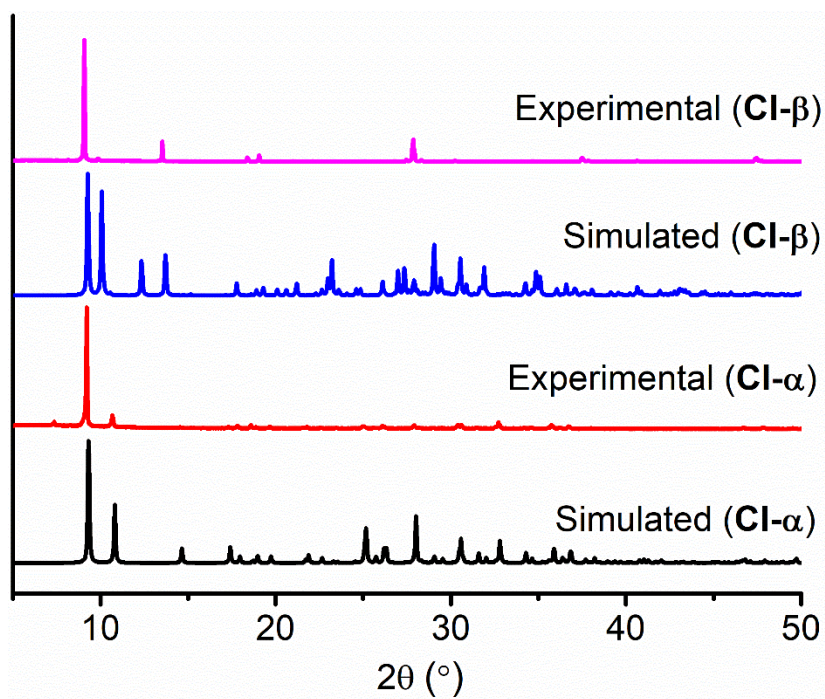
Fig. S1 Comparison of the experimental and simulated PXRD patterns of polymorphs. Note that the simulated patterns are extracted from the corresponding single-crystal X-ray data obtained at 300 K.
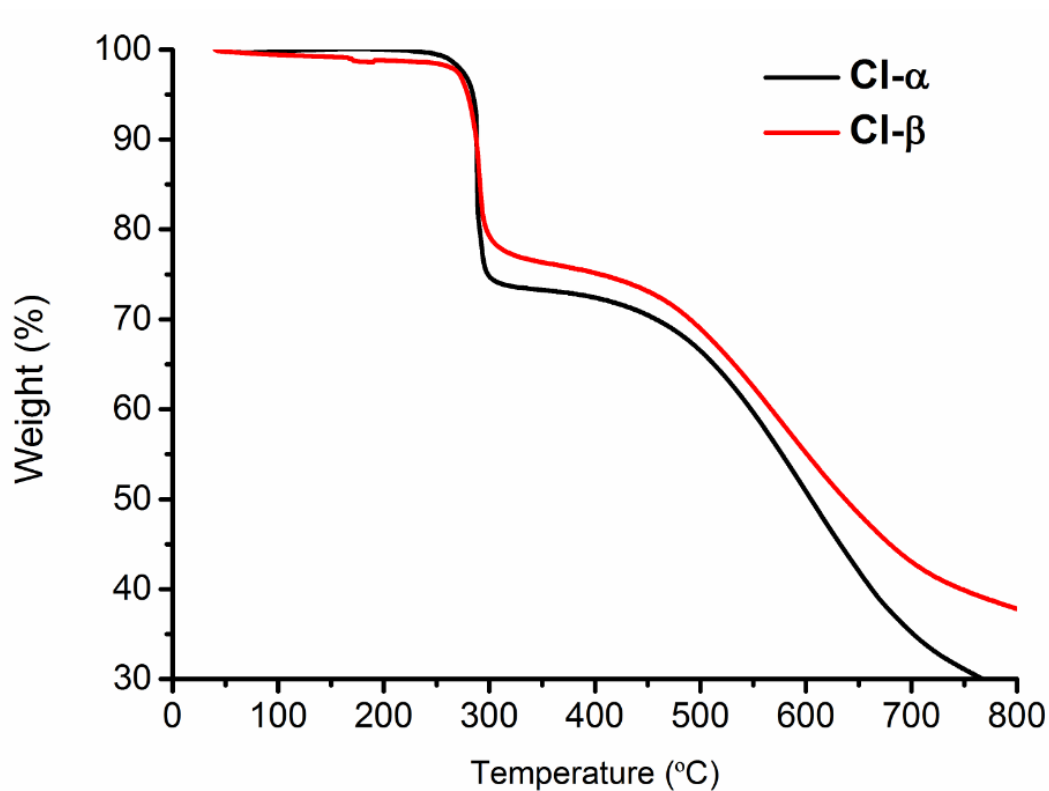

Fig. S2 Thermogravimetric analyses curves of **Cl-α** and **Cl-β**.

Crystal Data

Suitable single crystals of **Cl-α/Cl-β** were mounted with glue at the end of a glass fiber. Data collection was performed on an Oxford Diffraction XtalAB [Rigaku(Cu) X-ray dual wavelength source, Kα, $\lambda = 1.5418$ Å] equipped with a monochromator and CCD plate detector (CrysAlisPro CCD, Oxford Diffraction Ltd) at 150 K, 300 K. Structures were solved by direct methods by ShelXS[S1] in Olex2 1.2[S2] and refined on F^2 using full-matrix least-squares (SHELXL-2016/6[S1] in Olex2 1.2[S2]). All non-hydrogen atoms were refined with anisotropic thermal parameters, and all hydrogen atoms were included in calculated positions and refined with isotropic thermal parameters riding on those of the parent atoms. Crystal data and structure refinement parameters are summarized in Table S1. The crystals of the **Cl-α** form in *Pbcn* have cryatllographically-imposed twofold symmetry and that in the **Cl-β** form in *Pbca* with no cryatllographically imposed symmetry. CCDC Nos. 1889441-1889444.

Table S1 Summary of the structure refinement and crystallographic parameters

	Cl-α (150 K)	**Cl-α** (300 K)	**Cl-β** (150 K)	**Cl-β** (300 K)
Empirical formula	$C_9H_6Cu_3Cl_3N_6$	$C_9H_6Cu_3Cl_3N_6$	$C_9H_6Cu_3Cl_3N_6$	$C_9H_6Cu_3Cl_3N_6$
Formula weight	495.17	495.17	495.17	495.17
Temperature (K)	150.00(10)	300(2)	150.00(10)	300(1)
Wavelength (Å)	1.54184	1.54184	1.54184	1.54184
Crystal system	Orthorhombic	Orthorhombic	Orthorhombic	Orthorhombic
space group	*Pbcn*	*Pbcn*	*Pbca*	*Pbca*
a (Å)	16.3157(4)	16.3471(15)	17.3175(5)	17.5436(11)
b (Å)	11.6083(3)	11.6390(11)	8.5617(3)	8.6121(6)
c (Å)	7.6970(2)	7.8446(15)	18.9646(6)	19.0546(10)
Volume ($Å^3$)	1457.78(7)	1492.6(3)	2811.82(15)	2878.9(3)
Z	4	4	8	8
ρ_{calc} (g/cm^3)	2.256	2.204	2.339	2.285

F(000)	960	960	1920	1920
Theta range for data collection (°)	[4.675,77.328]	[4.664,78.961]	[4.663,77.831]	[4.641,77.809]
Total reflections	4789	5341	10541	9360
Unique reflections	1444	1488	2890	2916
R_{int}	0.0557	0.0961	0.0525	0.0456
Completeness (%)	97.1	96.5	99.2	98.5
Data / restraints / parameters	1444 / 0 / 97	1488 / 0 / 97	2890 / 0 / 190	2916 / 0 / 190
Goodness-of-fit on F^2	1.022	1.277	1.059	1.063
R_1[a] [I>2sigma(I)]	0.0538	0.0809	0.0526	0.0546
wR_2[b] (all data)	0.1428	0.3560	0.1511	0.1583
Largest diff. peak and hole (e/Å^3)	0.636, -0.544	0.807, -1.314	0.834, -0.822	0.619, -0.449

[a] $R_1 = \Sigma|F_o| - |F_c||/\Sigma|F_o|$. [b] $wR_2 = \{[\Sigma w(F_o^2-F_c^2)^2]/\Sigma[w(F_o^2)^2]\}^{1/2}$; $w = 1/ [\sigma^2(F_o^2) + (aP)^2 + bP]$, where $P = [\max(F_o^2,0) + 2F_c^2]/3$ for all data.

Table S2 Selected bond lengths (Å) and angles (°)

Cl-α (150 K)			
Cu(1)-N(1)	1.865(4)	Cu(1)-N(2)	1.860(4)
Cu(2)-N(3)	1.859(4)	--	--
N(2)-Cu(1)-N(1)	179.03(19)	N(3)-Cu(2)-N(3)#1	179.4(3)
Cl-α (300 K)			
Cu(1)-N(1)	1.870(8)	Cu(1)-N(2)	1.857(8)
Cu(2)-N(3)	1.859(10)	--	--
N(2)-Cu(1)-N(1)	178.6(5)	N(3)#1-Cu(2)-N(3)	180.0(5)
Cl-β (150 K)			
Cu(1)-Cu(2)#1	2.9150(11)	--	--
Cu(1)-N(2)	1.860(4)	Cu(1)-N(3)	1.864(5)
Cu(2)-N(5)	1.861(5)	Cu(2)-N(4)	1.873(5)
Cu(3)-N(6)	1.873(4)	Cu(3)-N(1)	1.868(5)
N(2)-Cu(1)-N(3)	175.8(2)	N(1)-Cu(3)-N(6)	175.8(2)

N(5)-Cu(2)-N(4)	175.7(2)	--	--
Cl-β (300 K)			
Cu(1)-Cu(2)#1	2.9706(12)	--	--
Cu(1)-N(2)	1.862(5)	Cu(1)-N(3)	1.863(5)
Cu(2)-N(4)	1.868(5)	Cu(2)-N(5)	1.865(5)
Cu(3)-N(1)	1.870(5)	Cu(3)-N(6)	1.866(5)
N(2)-Cu(1)-N(3)	176.1(2)	N(5)-Cu(2)-N(4)	176.1(2)
N(6)-Cu(3)-N(1)	176.0(2)	--	--

Symmetry code: For **Cl-α** (150 K) #1 -x+1, y, -z+1/2; For **Cl-α** (300 K) #1 -x+1, y, -z+1/2; For **Cl-β** (150 K) #1 -x, -y, -z+1; For **Cl-β** (300 K) #1 -x, -y+1, -z.

Table S3 Structural parameters related to supramolecular interactions (150 K)

Crystal	$d_{(Cu\cdots Cu, intra)}$[a] (Å)	$d_{(Cu\cdots Cu, inter)}$[a] (Å)	$d_{(Cu\cdots Cl)}$[b] (Å)	$d_{(C\cdots Cl)}$[c] (Å)	Angle $_{(C-H\cdots Cl)}$[c] (°)	Torsion Angle[d] (°)
Cl-α	3.24443(7) ~3.26519(7)	3.52981(8)	3.37382(9) ~3.45494(6)	3.63562(6) ~3.75789(7)	129.8696(12) ~132.7983(4)	3.55708(7) ~4.06732(8)
Cl-β	3.17891(8) ~3.27406(6)	2.9150(11)	3.16889(6) ~3.43789(7)	3.50231(10) ~3.95366(9)	115.013(2) ~129.3707(11)	5.27221(10) ~14.80595(15)

[a]Intra-and inter-molecular Cu···Cu distance; [b]Cu···Cl distance between molecules; [c]D···A distance and D-H··A angle for C-H···Cl hydrogen bonding, where D = C and A = Cl; [d]Torsion angle between Cu(I) trinuclear plane and pyrazole plane.

Table S4 Structural parameters related to supramolecular interactions (300 K)

Crystal	$d_{(Cu\cdots Cu, intra)}$[a] (Å)	$d_{(Cu\cdots Cu, inter)}$[a] (Å)	$d_{(Cu\cdots Cl)}$[b] (Å)	$d_{(C\cdots Cl)}$[c] (Å)	Angle $_{(C-H\cdots Cl)}$[c] (°)	Torsion Angle[d] (°)
Cl-α	3.2343(3) ~3.2380(3)	3.5414(5)	3.4199(3) ~3.5479(3)	3.6850(2) ~3.8257(4)	132.086(5) ~133.021(2)	2.3906(3) ~6.5844(7)
Cl-β	3.17315(15) ~3.2625(12)	2.9706(12)	3.21854(12) ~3.48095(16)	3.54907(18) ~3.96594(17)	116.513(3) ~130.381(2)	4.82003(18) ~14.4330(3)

[a]Intra-and inter-molecular Cu···Cu distance; [b]Cu···Cl distance between molecules; [c]D···A distance and D-H··A angle for C-H···Cl hydrogen bonding, where D = C and A = Cl; [d]Torsion angle between Cu(I) trinuclear plane and pyrazole plane.

150 K   300 K
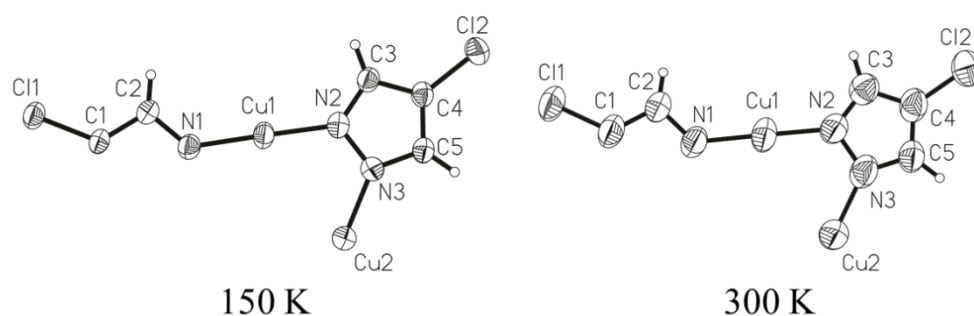
Fig. S3 The asymmetric units of **Cl-α** shown by ORTEP diagrams of 50% probability.
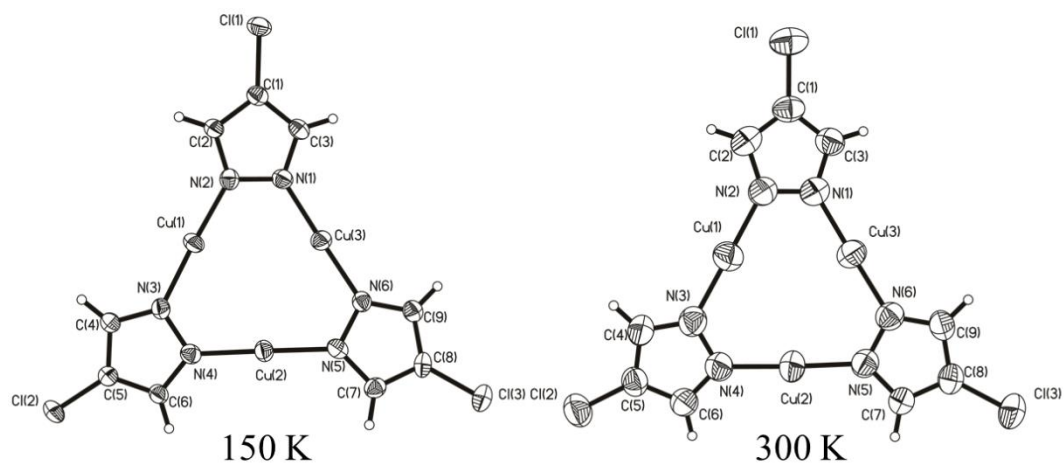
Fig. S4 The asymmetric units of **Cl-β** shown by ORTEP diagrams of 50% probability.
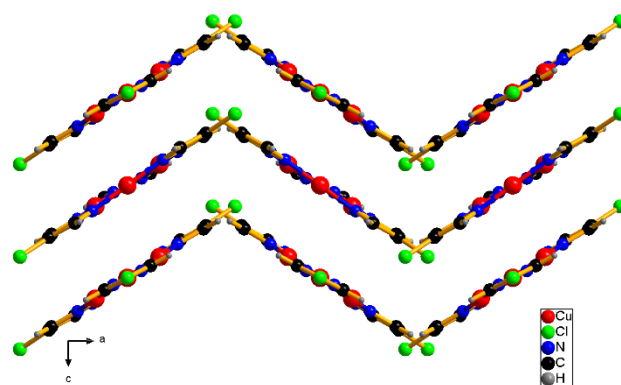
Fig. S5 Packing modes of **Cl-α** (300 K), showing the wave layer structure constructed by intralayer Cl-related non-covalent interactions.
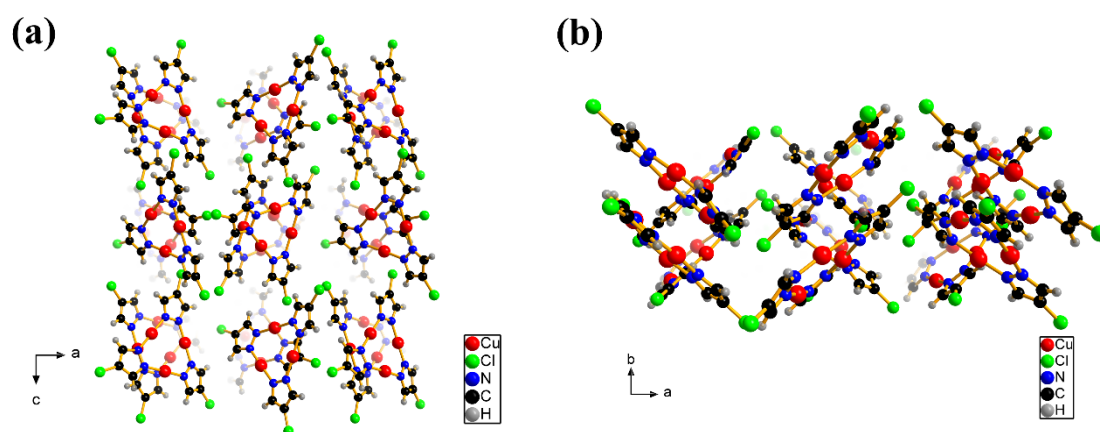
(a)

(b)

Fig. S6 Packing modes of **Cl-β** (300 K), showing the three-dimensional supramolecular framework along (a) the b axis and (b) the c axis.
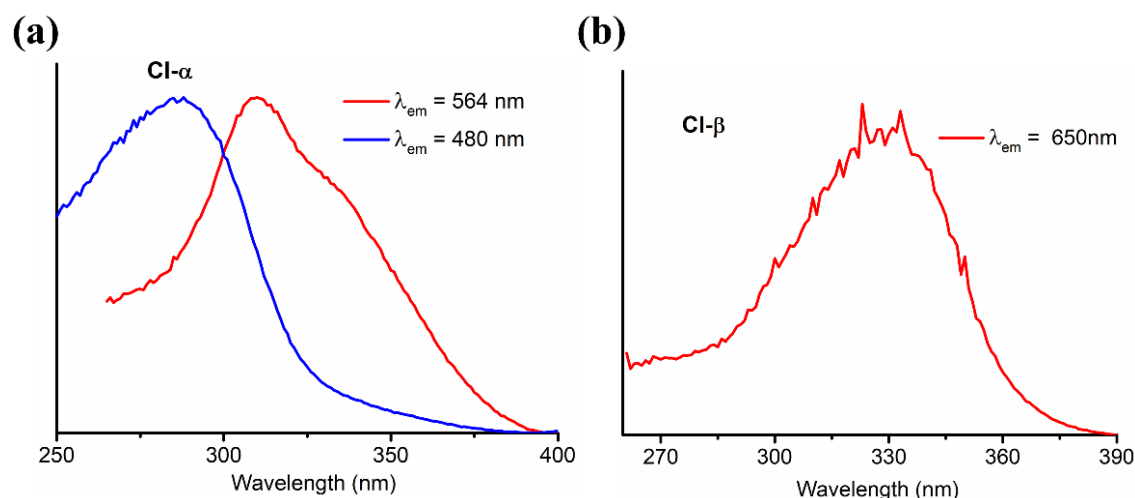
Photoluminescence data

Fig. S7 The solid-state excitation spectra of (a) **Cl-α**; (b) **Cl-β** at 300 K.

Table S5 The average emission lifetime (μs) of polymorphs in 77 K and 300 K

Polymorph	λ_{ex}	λ_{em}	77 K	300 K
Cl-α	290	480	55.98	19.84
	290	564	40.80	42.18
	310	480	47.99	21.56
	310	564	54.28	33.36
Cl-β	330	650	40.97	29.96
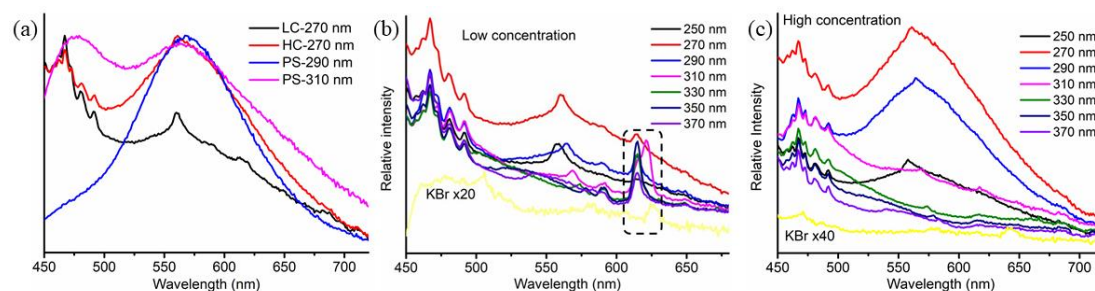
Fig. S8 The solid-state emission spectra for (a) low concentration (LC) and high concentration (HC) of **Cl-α** in KBr at 270 nm excitation, pure sample in **Cl-α** at 290 nm and 310 nm excitation (normalized); (b) LC at different excitation wavelength, dash rectangle indicates KBr sample peak; (c) HC at different excitation wavelength. Pure KBr was used as background and its spectra (yellow curve) were amplified 20 times in (b), 40 times in (c).
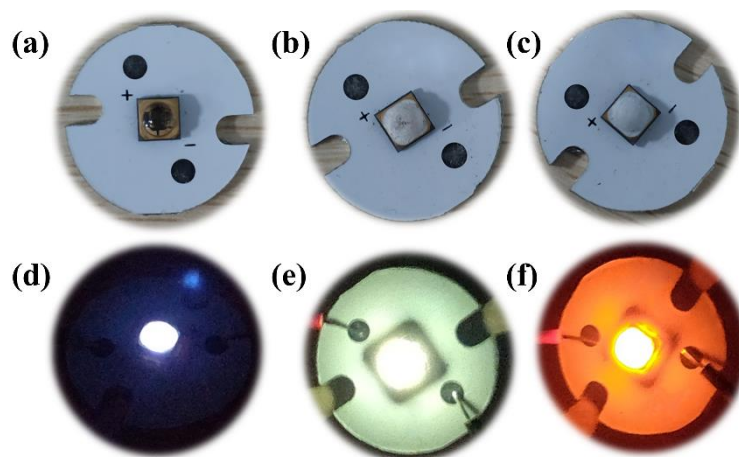
Fig. S9 Photographs of LEDs: (a) a 260 nm reference UV LED (commercially available); LED coated with a thin layer of (b) **Cl-α**, (c) **Cl-β**; (d) the not coated LED showing a purple light; (e) the LED coated with **Cl-α** illuminating bright yellow light. (f) the LED coated with **Cl-β** illuminating bright orange light.
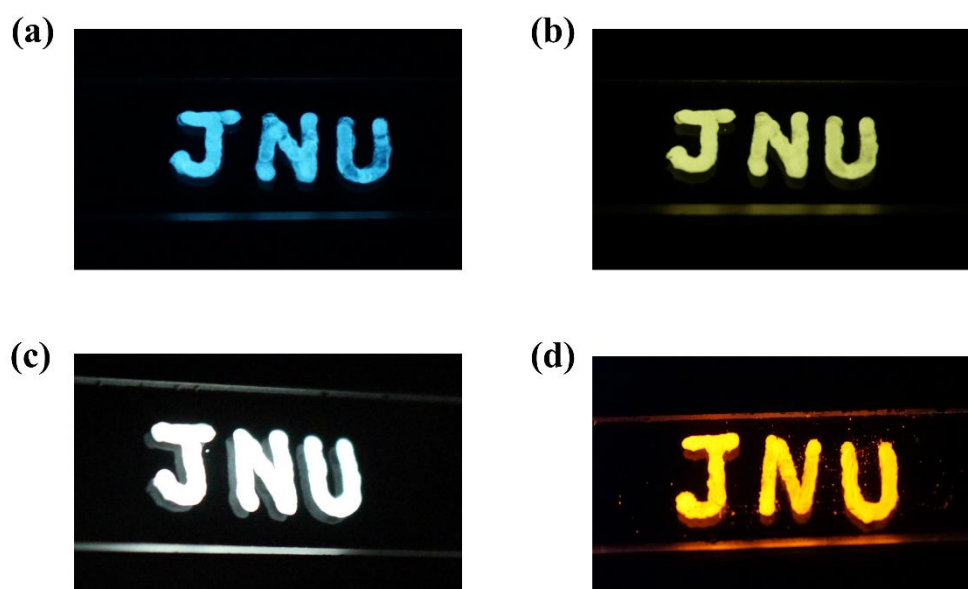
Fig. S10 Photographs of deposited polymorphs crystals on quartz glass (300 K): (a) **Cl-α** excited at 365 nm; (b) **Cl-α** excited at 254 nm, (c) **Cl-α** excited at 310 nm; (d) **Cl-β** excited at 330 nm.

Computational Detail

Non-covalent Interaction Analysis

Reduced density gradient (RDG) analysis is a convenient and cost-effective method for exploring supramolecular interactions, developed by Wei-Tao Yang et al[S3] and Tian Lu[S4]. Color-filled RDG isosurface between two interacting atoms or molecules indicate strong attraction (e.g. hydrogen bond), weak attraction (e.g. van der Waals interaction), weak repulsion, and strong repulsion by blue, green, brown, and red colors, respectively. Repulsion herein could be also expressed as steric hindrance.

The RDG analysis based on promolecular density embedded in Multiwfn 3.5[S4] allows our rapid non-covalent interaction analysis for large supramolecular unit taken from a crystal after inputting XYZ file of this supramolecular unit.

Herein, the supramolecular units containing a $[Cu(ClPz)]_3$ molecule and its surrounding molecules not connected by Cu $\cdots$ Cu interaction are chosen for both polymorphs at 300 K, in order to explore the supramolecular interactions orthogonal to intermolecular Cu $\cdots$ Cu bonding. The color-filled RDG isosurfaces were created in the cubic space centered at the geometrical center of the central $[Cu(ClPz)]_3$ molecule with extended distance for 23 Bohr in X, Y, Z direction, and the total grid numbers are 12167000 for both polymorphs.

Photophysical process

Density functional theory (DFT) and time-dependent DFT (TD-DFT) calculations were performed for clarifying photophysical process in both polymorphs.

All calculations were carried out using Gaussian 09 software package,[S5] and some of the output files were used as input files of Multiwfn 3.5 software packages[S4] to perform wave function analysis.

PBE0 functional[S6, S7] was used throughout unless otherwise mentioned, and effective core potential (ECP) of LanL2dz basis set was used for Cu and 6-31G** basis set was used for other atoms, based on the following calculated models:

(1) **M**: the optimized monomer of a $[Cu(ClPz)]_3$.

(2) **Cl-α-M**: the monomer taken from the X-ray structure of **Cl-α** at 150 K.

(3) **Cl-β-M**: the monomer taken from the X-ray structure of **Cl-β** at 150 K.

(4) **D**: the optimized geometry of chair dimer of $[Cu(ClPz)]_3$ from the **Cl-α** at 150 K , displaying intermolecular Cu···Cu interaction.

(5) **Cl-α-D**: the dimer taken from the X-ray structure of **Cl-α** at 150 K, displaying intermolecular Cu···Cu interaction.

(6) **Cl-β-D**: the dimer taken from the X-ray structure of **Cl-β** at 150 K, displaying intermolecular Cu···Cu interaction.

(7) **Cl-α-D(Cl)**: the dimer of $[Cu(ClPz)]_3$ taken from the X-ray structure of **Cl-α** at 150 K, displaying the Cu ···Cl, Cl ···H-C interaction. The TDDFT results for this additional model (Table S20) shows that both the lowest-energy singlet and triplet excited states (S_1 and T_1) locate in only one $[Cu(ClPz)]_3$ molecule, confirming that the low-energy excimeric phosphorescence arise from the excimer formed by intermolecular Cu···Cu bonding but Cl-involved interactions.

Electron density difference (EDD) maps (isovalue = 5.0×10^{-4} a.u.) were obtained to provide accurate assignments of excited states by calculating the first 20 singlet-singlet spin-allowed transitions and the first 40 singlet-triplet spin-forbidden transitions with IOp(9/40=4) and then the results were further treated by Multiwfn 3.5 software packages[S4] using the formatted checkpoint file (fchk files) as well as the Gaussian output file (log files) as input files.

Oscillator strengths are denoted as *f*. MMCT = metal-metal charge transfer; ILCT = intraligand charge transfer; MLCT = metal-to-ligand charge transfer; LMMCT = ligand-to-metal-metal-bonding charge transfer.

Note that the models without optimization are taken from X-ray data at 150 K rather than at 300 K for higher quality of crystal data, but the key structural parameters are very similar in both temperatures.

The key intramolecular structural parameters for both polymorphs at either 300 K or 150 K have been well-reproduced in optimized geometries, and the intermolecular Cu ···Cu distances lie between those of **Cl-α** and **Cl-β** at either temperature (Table S6).

For confirming that TD-PBE0 functional is suitable for our systems, M06-2X[S8] and

ωB97XD[S9] functional, which are usually considered to be more suitable for charge-transfer excited states than PBE0, are used in TD-DFT calculations for calculating the lowest-lying spin-allowed and spin-forbidden transitions based on the monomer and chair dimer models for **Cl-α** at 150 K. The results (Table S7) show that PBE0 functional seems more suitable for our systems, because the calculated lowest-lying transition energies PBE0 are the closest to experimental excitation wavelengths among the above three functionals. Moreover, the assignments of excited states indicated by EDD maps show neglectable difference for the same electronic states based on the same models between these functionals, except for the T_1 state of monomer show the largest contributions from ligands at ωB97XD level.
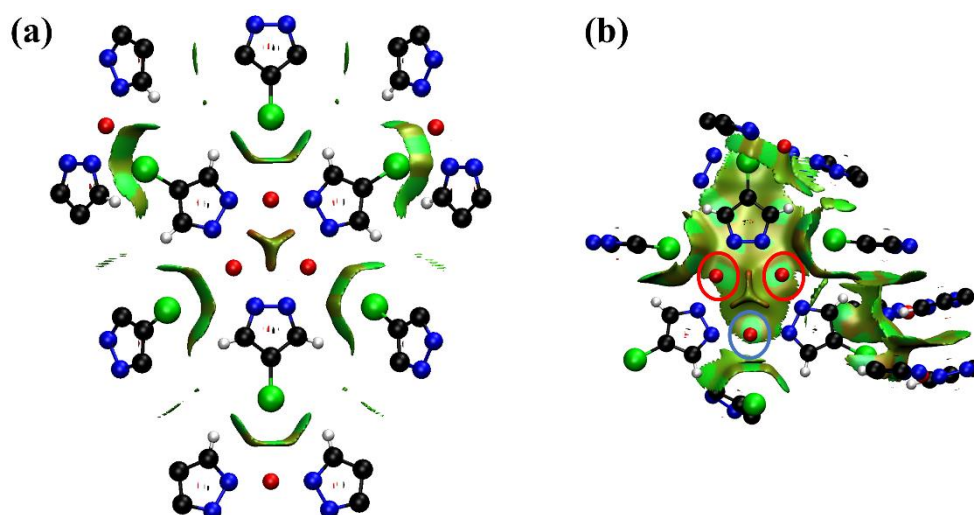
Fig. S11 Color-filled RDG isosurfaces for polymorphs (isovalue = 0.5 a.u.) at 300 K, showing the supramolecular interaction related to Cl, (a) **Cl-α;** (b) **Cl-β**, red circle means the Cu atoms interact with pyzaolate of adjacent molecule, while the blue circle means the interaction between the Cu atoms and Cl atoms. Green isosurfaces between molecules indicates Cu···Cl and C-H···Cl interactions in the level of van der Waals attraction, while brown isosurfaces indicates weak steric hindrance (ranging from -0.03 to 0.02 a.u.).

Table S6 The comparison between X-ray data and optimized geometries of polymorphs

	M	**D**	**Cl-α** (150 K)	**Cl-β** (150 K)	**Cl-α** (300 K)	**Cl-β** (300 K)
$d_{(Cu \cdots Cu,intra)}$ (Å)	3.249 ~3.250	3.245 ~3.256	3.244 ~3.265	3.179 ~3.274	3.234 ~3.238	3.173 ~3.263
$d_{(Cu \cdots Cu,inter)}$ (Å)	--	3.167, 3.167, 3.254, 3.254	3.530, 3.530	2.915, 2.915	3.541, 3.541	2.970 2.970
N-Cu-N(°)	179.5 ~179.6	172.6 ~176.7	179.0 ~179.4	175.7 ~175.8	178.6 ~180.0	176.0 ~176.1
Torsion Angle[a] (°)	0	3.91	3.56	5.27	2.39	4.82
	0	7.42	3.56	14.58	2.39	13.47
	0	8.31	4.06	14.80	6.58	14.43

[a]Torsion angle between trinuclear plane and pyrazole plane
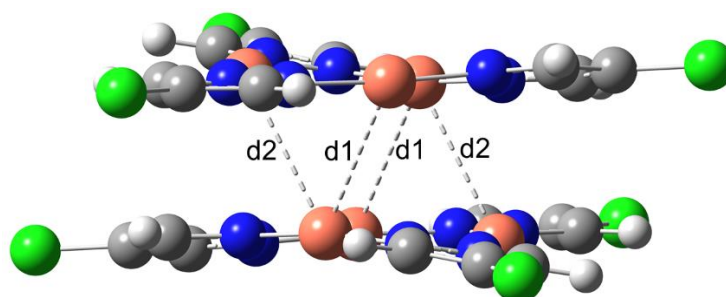
Fig. S12 The optimized geometry for the dimer (**D**), showing two kinds of intermolecular Cu···Cu contacts with the distances of 3.254 Å (d1) and 3.167 Å (d2), respectively.
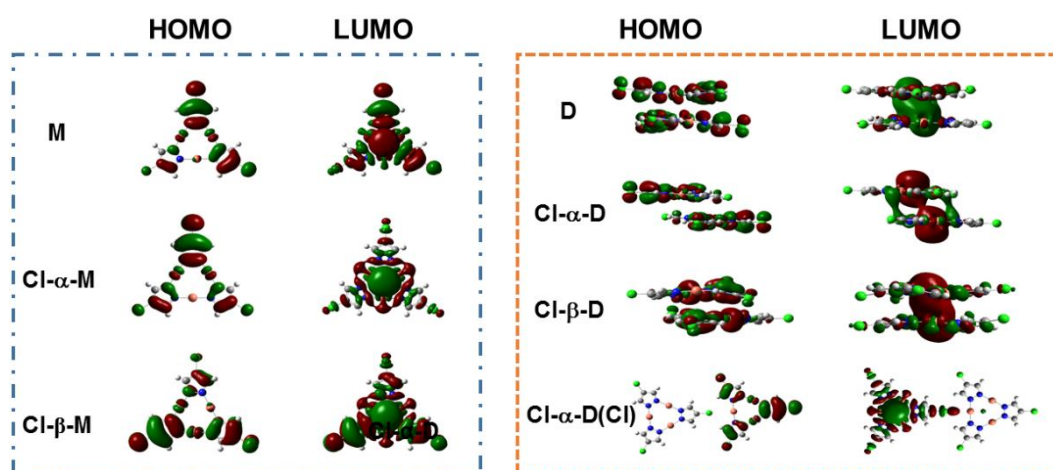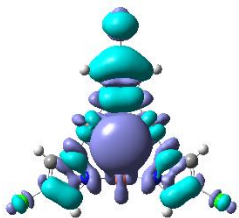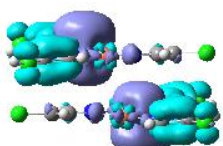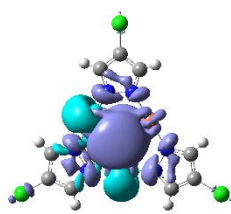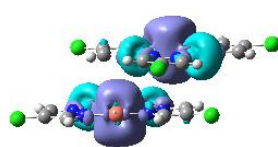
Fig. S13 The frontier molecular orbitals (isovalue = 0.02)

Comment:

The HOMO in each model consists of the π* orbitals of the pyrazolates and the d orbitals of the Cu(I) ions, while the LUMO is the typical Cu⋯Cu bonding orbital. These features are similar to those of Cu_3Pz_3 without any aromatic substituents, although p–π conjugation between Cl and the pyrazolyl ring increases ligand participation in the FMOs of $[Cu(ClPz)]_3$.

Table S7 Comparison for TDDFT results with various functionals based on the monomer and dimer models taken from X-ray data for **Cl-α** at 150 K

		Monomer	Dimer
PBE0	S_1	E = 4.697 eV, λ= 264.1 nm, f=0.00	E = 4.771 eV, λ= 260.1 nm, f=0.00
	T_1	E = 4.106 eV, λ= 302.2 nm	E = 4.099 eV λ= 302.7 nm
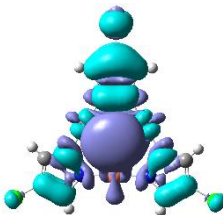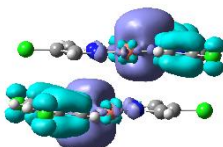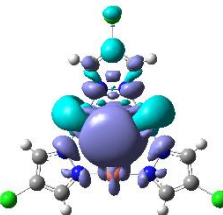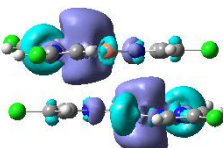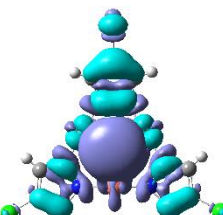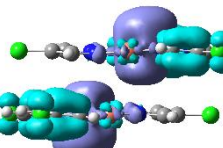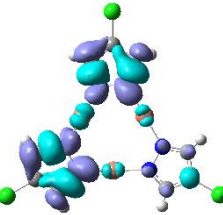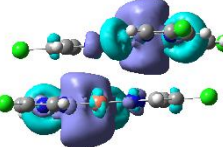
M06-2X	S$_1$	 E = 5.190 eV, λ= 239.0 nm f =0.00	 E = 5.238 eV, λ= 236.0 nm f =0.00
	T$_1$	 E = 4.663 eV, λ= 266.1 nm	 E = 4.619 eV, λ= 268.6 nm
ωB97XD	S$_1$	 E = 5.213 eV, λ= 238.0 nm f =0.00	 E = 5.238 eV, λ= 236.9 nm f =0.00
	T$_1$	 E = 4.501 eV, λ= 275.6 nm	 E = 4.619 eV, λ= 268.6 nm

Table S8 Comparation of maximum oscillator strengths between the [Cu(ClPz)]₃ and [Cu(EBP)]₃[a] among the first 10 singlet-singlet spin-allowed transitions at TD-PBE0/(LanL2dz for Cu and 6-31G** for other atoms) level

	Monomer	Dimer[c]
[Cu(ClPz)]₃ (optimized)	0.04	0.07
Cl-α[b]	0.03	0.04
Cl-β[b]	0.03	0.07
[Cu(EBP)]₃	1.05	0.96

[a]reference S10. EBP = ethyl-4′-benzoate-3,5-dimethylpyrazolate. [Cu(EBP)]₃ is complex **1** in reference S10. [b]Taken from SCXRD data at 150 K. [c]Chair dimers.
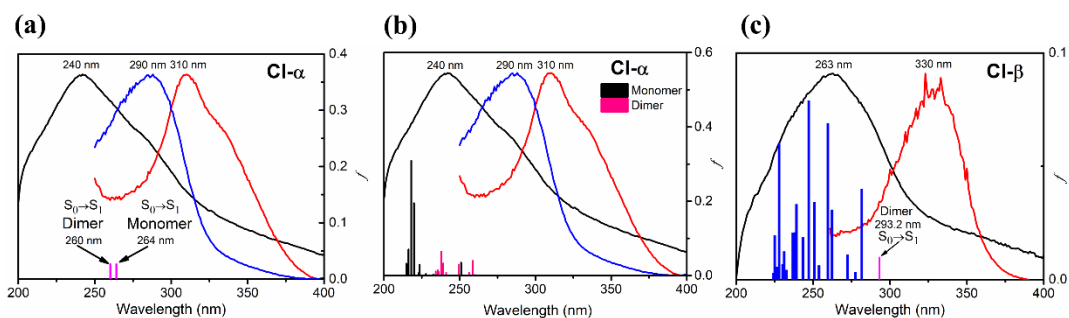
Fig. S14 The experimental UV-Vis absorption (black curve) and excitation spectra (blue and red curves) in comparison with the simulated UV-Vis absorption spectra of (a) showing only $S_0 \rightarrow S_1$ transitions for a monomer and a dimer denoted only their wavelengths but oscillator strengths by two magenta columns, and (b) all our simulated singlet-singlet transitions for a monomer and a chair dimer for **Cl-α**. (c) The experimental UV-Vis absorption (black curve) and excitation spectra (red curve) in comparison with the simulated UV-Vis absorption spectra (blue columns) of a chair dimer for **Cl-β**, and the magenta column denotes the wavelength of $S_0 \rightarrow S_1$ transition but oscillator strength.

Comment:

Compared with our previously reported [Cu(EBP)]₃, the oscillator strengths for [Cu(ClPz)]₃ are much smaller among the first 10 singlet excited states (Table S7). Besides, the experimental optimal excitation wavelengths for triggering yellow, white, or blue light for **Cl-α** and orange light for **Cl-β**, lie in the weak absorption regions in their UV-Vis absorption spectra (Fig. S14), indicating these optimal excitations are weak allowed transitions. As a result, it seems reasonable to propose that the excitations at 270 nm and 310 nm for **Cl-α** corresponds to $S_0 \rightarrow S_1$ transitions of a dimer and a monomer, respectively, although their oscillator strengths are quite close to 0. Moreover, since the 330 nm excitation for blue light is weaker than 310 nm for white light, the 330
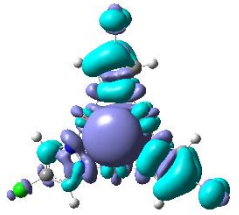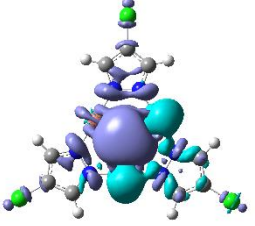
nm is more likely a spin-forbidden monomeric $S_0 \rightarrow T_1$ excitation. Previously, Omary and Dias have figured out that the bright orange light for $\{Cu[3,5-(CF_3)_2-Pz)]\}_3$ arise from a spin-forbidden excitation, based on their comprehensive spectroscopic evidences.[S11] The optimal excitation ($\lambda_{ex} = 330$ nm) for orange light of **Cl-β** should arise from the $S_0 \rightarrow S_1$ transitions of a dimer. Indeed, the calculated wavelengths for $S_0(M) \rightarrow T_1(M)$ transitions are 260 nm for **Cl-α** and 293 nm for **Cl-β,** consistent with the order of experimental excitations (270 nm for **Cl-α** and 330 nm for **Cl-β**).

Table S9 The comparison between X-ray data at 300 K and optimized geometries (S_0 and T_1) of polymorphs

	Cl-α (300 K)	**Cl-β** (300 K)	S_0	T_1[a]
$d_{(Cu \cdots Cu, intra)}$ (Å)	3.234 ~3.238	3.172 ~3.263	3.245 ~3.256	2.653 ~3.089
$d_{(Cu \cdots Cu, inter)}$ (Å)	3.541, 3.541	2.970, 2.970	3.167, 3.167, 3.254, 3.254	

[a]The geometry of the chair dimer in T_1 state was optimized at unrestricted PBE0 level, resulting in the typical $Cu \cdots Cu$ bonding excimer, suggested by the significant shorter $Cu \cdots Cu$ distances compared with those in the optimized S_0 state.

Table S10 TDDFT results of selected $S_0 \rightarrow S_n$ transitions for **M**

No.	λ (nm)	E (eV)	f	EDD	Assignment
1	268.3	4.625	0.00		[1]LMMCT/ [1]ILCT/
3	255.9	4.849	0.04		[1]MMCT/ [1]MLCT/ [1]ILCT
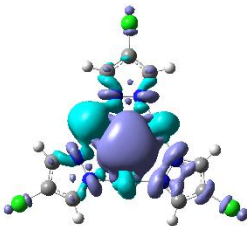
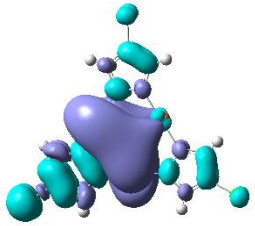| No.	λ (nm)	E (eV)	f	EDD	Assignment
4	255.8	4.850	0.04		[1]LMMCT

Table S11 TDDFT results of selected $S_0 \rightarrow T_n$ transitions for **M**
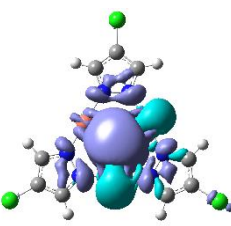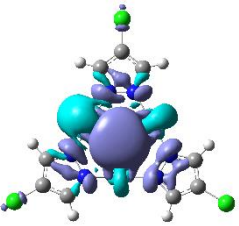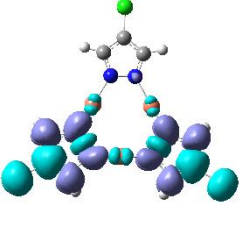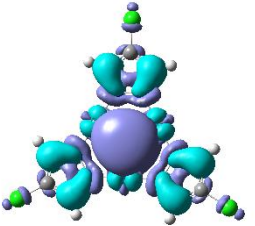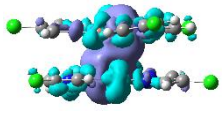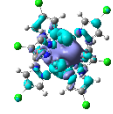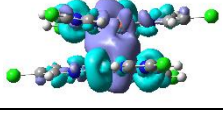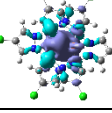
No.	λ (nm)	E (eV)	EDD	Assignment
1	313.2	3.961		[3]MMCT/ [3]MLCT
2	313.1	3.962		[3]MMLCT
11	268.9	4.615		[3]MLCT
12	260.4	4.765		[3]LMMCT

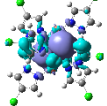**Table S12** TDDFT results of selected $S_0 \rightarrow S_n$ transitions for **D**

No.	λ (nm)	E (eV)	f	EDD		Assignment
				Side view	Top view	
1	305.2	4.065	0.00			[3]MMCT
3	298.8	4.153	0.01			[3]MMCT
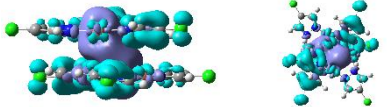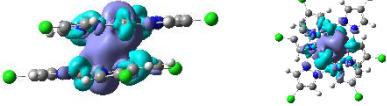
No.	λ (nm)	E (eV)	f	EDD	Assignment
7	290.9	4.265	0.03		[3]LMMCT
8	282.0	4.440	0.07		[3]LMMCT
10	272.8	4.550	0.06		[3]MMCT

Table S13 TDDFT results of selected $S_0 \rightarrow T_n$ transitions for **D**
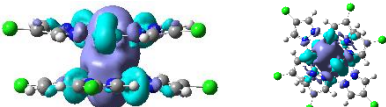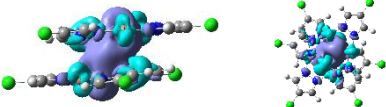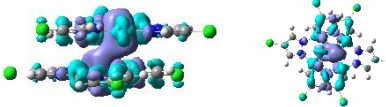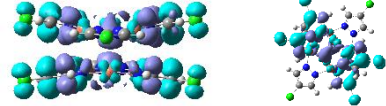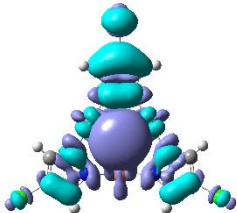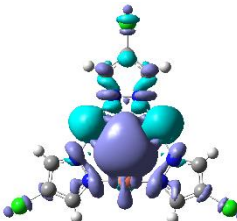
No.	λ (nm)	E (eV)	EDD		Assignment
			Side view	Top view	
1	362.8	3.420			[3]MMCT
7	301.0	4.122			[3]LMMCT
10	289.5	4.286			[3]MMCT
14	282.1	4.398			[3]LMMCT
22	273.6	4.535			[3]ILCT

Table S14 TDDFT results of selected $S_0 \rightarrow S_n$ transitions for **Cl-α-M**

No.	λ (nm)	E (eV)	f	EDD	Assignment
1	264.1	4.697	0.00		[1]LMMCT/ [1]ILCT
3	251.0	4.944	0.03		[1]MMCT/ [1]ILCT
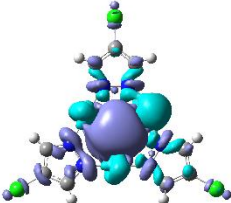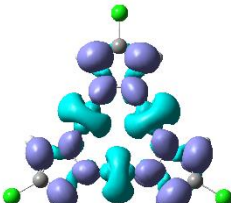
No.	λ (nm)	E (eV)		EDD	Assignment
4	251.0	4.944	0.03		[1]MMLCT
10	223.6	5.549	0.03		[1]MLCT

Table S15 TDDFT results of selected $S_0 \rightarrow T_n$ transitions for **Cl-α-M**
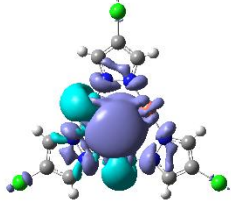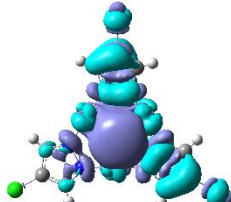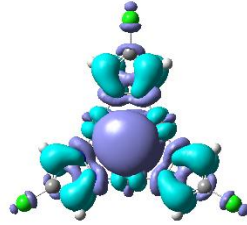
No.	λ (nm)	E (eV)	EDD	Assignment
1	302.2	4.106		[3]MMCT/ [3]MLCT
11	268.3	4.624		[3]LMMCT/ [3]ILCT
12	252.3	4.919		[3]LMMCT
27	224.2	5.534		[3]LMMCT/ [3]ILCT

Table S16 TDDFT results of selected $S_0 \rightarrow S_n$ transitions for **Cl-α-D**
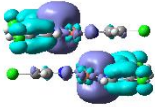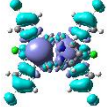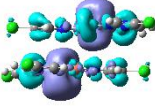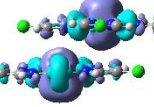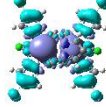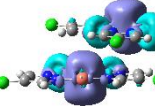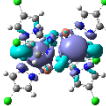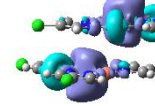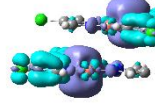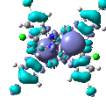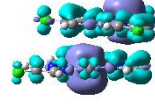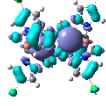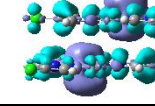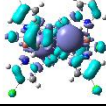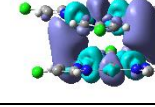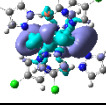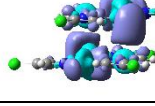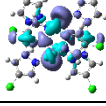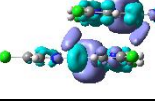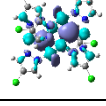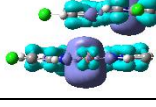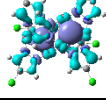
No.	λ (nm)	E (eV)	f	EDD		Assignment
				Side view	Top view	
1.	260.1	4.771	0.00			[1]LMMCT
3	258.7	4.797	0.04			[3]LMMCT
8	249.6	4.972	0.03			[3]LMMCT

Table S17 TDDFT results of selected $S_0 \rightarrow T_n$ transitions for **Cl-α-D**

No.	λ (nm)	E (eV)	EDD		Assignment
			Side view	Top view	
1	302.7	4.099			[3]MMCT
2	302.4	4.102			[3]MMCT
20	267.0	4.647			[3]LMMCT
21	263.4	4.711			[3]LMMCT
22	262.7	4.724			[3]LMMCT
23	258.2	4.805			[3]MMCT
24	252.0	4.924			[3]MMCT
25	249.3	4.976			[3]LMMCT
26	249.1	4.980			[3]LMMCT

| 27 | 248.3 | 4.997 | | ^{3}LMMCT/ ^{3}MMLCT |

Table S18 TDDFT results of selected $S_0 \rightarrow S_n$ transitions for **Cl-β-M**
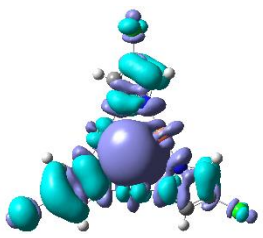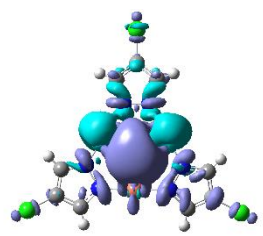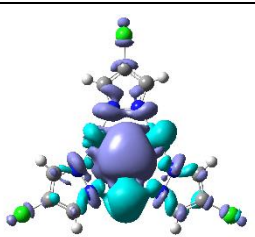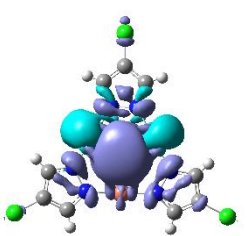
No.	λ (nm)	E (eV)	f	EDD	Assignment
1	265.0	4.681	0.00		^{1}MMCT/ ^{1}ILCT
3	254.0	4.884	0.04		^{1}MMCT
4	252.2	4.919	0.04		^{1}MMLCT/ ^{1}ILCT
9	224.1	5.537	0.02		^{1}MLCT

Table S19 TDDFT results of selected $S_0 \rightarrow T_n$ transitions for **Cl-β-M**

No.	λ (nm)	E (eV)	EDD	Assignment
1	308.5	4.021		^{3}MMCT
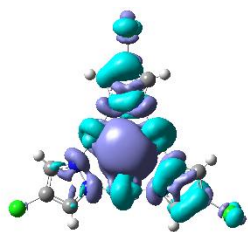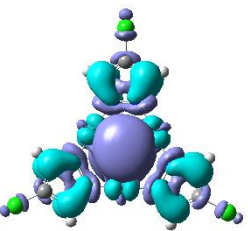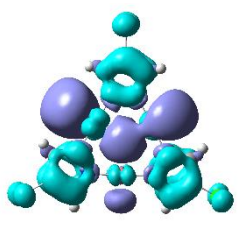
11	270.8	4.582		^{3}MMCT/ ^{3}ILCT
12	255.3	4.860		^{3}MMLCT/ ^{3}ILCT
26	224.9	5.516		^{3}LMMCT

Table S20 TDDFT results of selected $S_0 \rightarrow S_n$ transitions for **Cl-β-D**
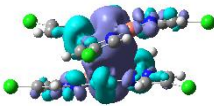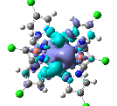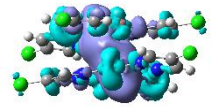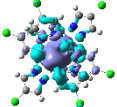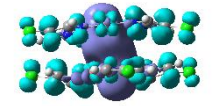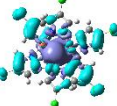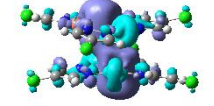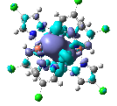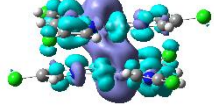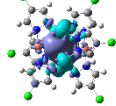
No.	λ (nm)	E (eV)	f	EDD		Assignment
				Side view	Top view	
1	293.2	4.232	0.00			^{1}MMCT/ ^{1}ILCT
3	281.7	4.405	0.04			^{1}LMMCT
6	272.4	4.556	0.01			^{1}LMMCT
8	262.4	4.729	0.03			^{1}MMCT
9	259.6	4.779	0.07			^{1}LMMCT

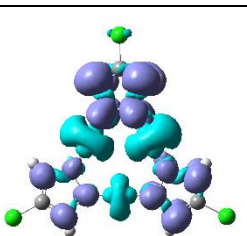**Table S21** TDDFT results of selected $S_0 \rightarrow T_n$ transitions for **Cl-β-D**

No.	λ (nm)	E (eV)	EDD		Assignment
			Side view	Top view	
1	343.1	3.616			^{3}MMCT
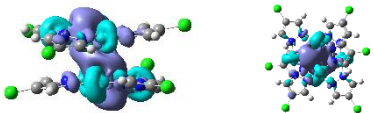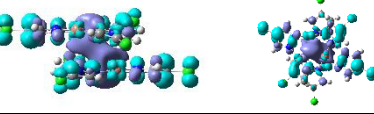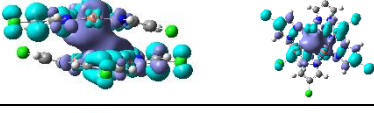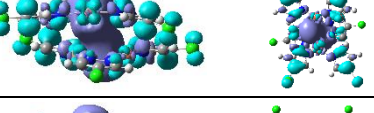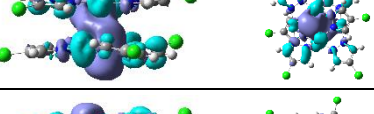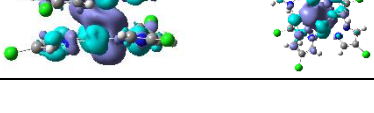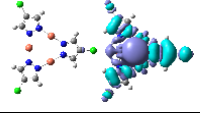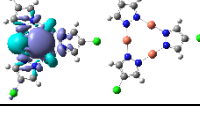
2	328.1	3.782		[3]MMCT
14	282.8	4.388		[3]LMMCT
15	282.2	4.397		[3]LMMCT
21	273.9	4.529		[3]LMMCT
24	262.1	4.734		[3]LMMCT
25	259.8	4.775		[3]LMMCT

Table S22 Selected TDDFT results of **Cl-α-D(Cl)**, showing that the non-covalent interactions related to Cl does not take part in the lowest-lying transitions.

Selected state	λ (nm)	E (eV)	f	EDD	Assignment
$S_0 \rightarrow S_1$	264.0	4.700	0.00		[1]LMMCT
$S_0 \rightarrow T_1$	303.0	4.095	0.00		[3]MMCT
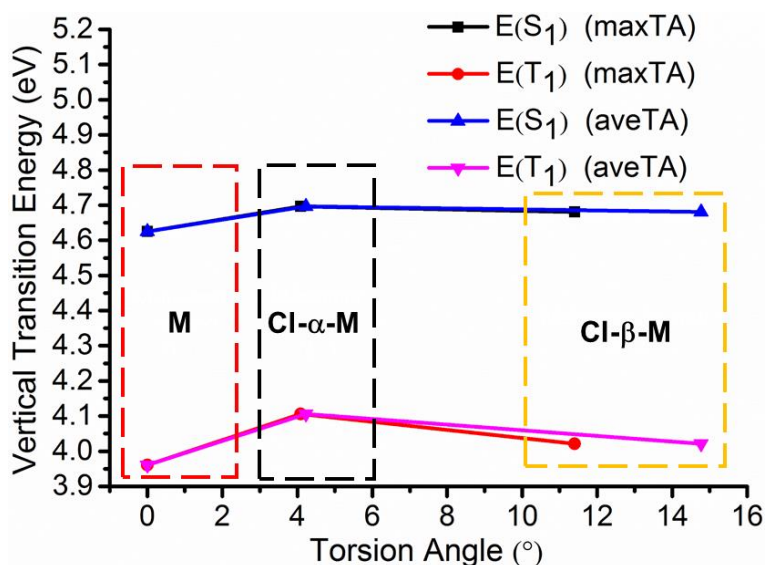
Fig. S15 The lowest-lying singlet-singlet and singlet-triplet vertical transition energies for the monomers in the optimized geometry (**M**), the single crystal of **Cl-α** at 150 K (**Cl-α-M**) and the single crystal of **Cl-β** at 150 K (**Cl-β-M**), showing the relationship between the energies of excited states and the maximum and average torsion angle (denoted as maxTA and aveTA, respectively).
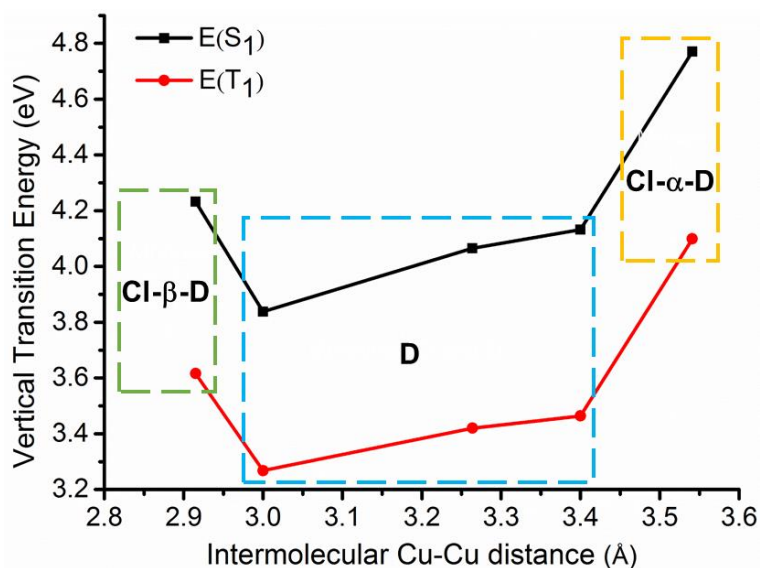
Fig. S16 The lowest-lying singlet-singlet and singlet-triplet vertical transition energies for the dimers in the optimized geometry and its modified versions (**D**), the single crystal of **Cl-α** at 150 K (**Cl-α-D**) and the single crystal of **Cl-β** at 150 K (**Cl-β-D**), showing the increasing energies of excited states following by the increasing intermolecular Cu···Cu distances. Herein, the data points denoted as **D** in the blue box refer to the transition energies for the optimized geometry (d1 = 3.254 Å) and its modified versions by simply changing d1 to 3.200 Å and 3.400 Å, respectively. See Fig. S12 for d1. Although the distorted molecular conformations in **Cl-β-D** results in the higher-lying S_1 and T_1 states than those for **D**, its energies are still much lower than those for **Cl-α-D**.

Literature survey for Cu₃pyrazolate₃

Table S23 Summary of intra- and inter-molecular Cu⋅⋅Cu distance of cyclic Cu₃pyrazolate₃ for polymorphs.

The pyrazolate ligand	T(K)	$d_{(Cu⋅⋅Cu, intra)}$ (Å)	$d_{(Cu⋅⋅Cu, inter)}$ (Å)	Ref.	
3,5-dimethyl-pyrazolate	295	3.195~3.258	2.944(2), 2.947(2)	S12	Polymorphs
	298	3.1950(5)~3.2582(5)	2.9534(5), 2.9534(5)	S13	
4-(4-bromophenyl)-3,5-dimethyl-pyrazolate (**Br-α**)	293	3.1617(14)~3.2570(14)	2.8622(15)	S14	Polymorphs
	100	3.1523(9)~3.2741(9)	2.8174(9)		
4-(4-bromophenyl)-3,5-dimethyl-pyrazolate (**Br-β**)	100	3.1435(47)~3.2784(50)	3.020(3), 3.038(4)		
ethyl-4′-benzoate-3,5-dimethyl-pyrazolate (**2a**)	293	3.160(2)~3.230(2)	3.135(2), 3.141(2)	S10	Polymorphs
ethyl-4′-benzoate-3,5-dimethyl-pyrazolate (**2b**)	293	3.158(2)~3.245(3)	3.124(2), 3.124(2), 3.171(3), 3.171(3)		
ethyl-4′-benzoate-3,5-dimethyl-pyrazolate (**2c**)	293	3.1781(6)~3.2244(6)	3.0885(6), 3.0885(6)		

Table S24 Summary of luminescent data for halogen cyclic Cu₃pyrazolate₃

The pyrazolate ligand	d(Cu-Cu) (Å)[b]	T_{cry} (K)[c]	λ_{em} (nm)[d]	T_{em} (K)[e]	Drawback[f]	Ref.
4-iodo-3,5-dimethyl-pyrazolate	3.631(4), 3.897(4)	293	621	293	(1)	S15
			630	77		
4-(4-bromophenyl)-3,5-dimethylpyrazolate (**Br-α**)[a]	2.8622(15)	293	670	RT	(2)	S14
	2.8174(9)	100				
4-(4-bromophenyl)-3,5-dimethylpyrazolate (**Br-β**)[a]	3.020(3), 3.038(4)	100	670	RT	(2)	
4-bromo-3,5-	> 5.0	296	574	RT	(3)	S16

bis(trifluoro-methyl)pyrazolate			582	77		
4-chloro-3,5-bis(trifluoro-methyl)pyrazolate		296	580	RT		
			590	77		

[a]A pair of genuine polymorphs; [b]Intermolecular Cu⋯Cu distance; [c]Determination temperature for single-crystal X-ray diffraction; [d]Emission maximum; [e]Determination temperature for luminescent property; [f]The disadvantage for producing comparable high-energy and low-energy emission bands as follows: (1) although the Cu⋯Cu distances are too long to form Cu⋯Cu interaction, the excimer formation is still quite favorable due to the lack of rigid restriction from supramolecular interaction, leaving only excimeric low-energy band, (2) the quite short or moderate Cu⋯Cu distances facilitate the direct population for excited dimers, leaving only low-energy band, (3) the Cu-Cu distances are too long to form excimeric Cu⋯Cu bonding, as suggested in reference S16, but a reasonable assignment for the low-energy bands have not yet been provided.

Table S25 Photophysical data determined at around room temperature (RT) for solid-state samples of our Polymorphs and previously reported Cu₃pyrazolate₃[a]

Complex	T (K)	λ_{ex} (nm)	λ_{em} (nm)	τ_{av} (μs)	QY(%)	k_r (10^2 s^{-1})	k_{nr} (10^2 s^{-1})	Ref.
Cl-α	300	290	564	42.18	76.6	181.60	55.95	This work
Cl-β	300	330	650	29.96	78.2	261.01	72.76	
[Cu(L1)]₃[b]	RT	254	631	42.8	90	210.28	23.36	S17
[Cu(L2)]₃[c]	293	280	570	30.5	84	275.40	52.46	S15
[Cu(L3)]₃[d]	293	280	621	21.7	62	285.71	175.11	

[a]Only those providing both emission decay times (τ) and absolute quantum yield (QY) are summarized in this table, so that both radiative rate (k_r) and non-radiative rate (k_{nr}) could be calculated to be discussed. [b]HL₁ = 4-hexyl-3,5-dimethylpyrazole. The photophysical data for [Cu(L₁)]₃ are determined in poly(methyl methacrylate) (PMMA) doped films. [c]HL₂ = 3,5-dimethyl-4-bromopyrazole. [d]HL₃ = 3,5-dimethyl-4-iodopyrazole.

Comment:

Herein, we confirmed that, for both polymorphs, rigid supramolecular networks constructed by non-covalent interactions related to Cl could facilitate high QYs (near 80%) by reducing vibrational relaxation, resulting in small non-radiative rate (k_{nr}). By comparing the room-temperature phosphorescent data with other Cu₃Pz₃, it was found that reducing k_{nr} may be somewhat more effective than raising radiative rate (k_r) for obtaining high QYs. For instance, [Cu(3,5-dimethyl-4-iodopyrazole)]₃ displays lower QY (62%) than our polymorphs herein (78.2% for the yellow light of Cl-α and 76.6% for the orange light of Cl-β), because its k_{nr} (17511 s^{-1}) is much larger than our cases

(5595 s^{-1} for **Cl-α** and 7276 s^{-1} for Cl-β), although its k_r (28571 s^{-1}) is also larger (18160 s^{-1} for **Cl-α** and 26101 s^{-1} for Cl-β). In contrast, the highest QY (90%) among Cu_3Pz_3 was the one with 4-hexyl-3,5-dimethylpyrazolate doped in a poly(methylmethacrylate) (PMMA) film,[S17] exhibiting the k_{nr} as low as 2336 s^{-1} due to a rigid environment, although its k_r (21028 s^{-1}) is close to that of Cl-α and significantly smaller than that of Cl-β. Besides, the rigid networks seem inhibit noticeable shortening of intermolecular Cu···Cu distances when cooling, resulting in neglectable shifting of emission bands. In contrast, significant red-shifting (e.g., up to 100 nm) are usually observed for Cu_3Pz_3 when cooling from room temperature to 77 K, through enhancing Cu···Cu bonding during lattice contraction.[S11]

Reference

S1 G. M. Sheldrick, *Acta Cryst. A*, 2008, **64**, 112-122.

S2 O.V. Dolomanov, L. J. Bourhis, R. J. Gildea, J. A. K. Howard and H. Puschmann, *J. Appl. Cryst.*, 2009, **42**, 339-341.

S3 E. R. Johnson, S. Keinan, P. Mori-Sanchez, J. Contreras-Garcia, A. J. Cohen and W. Yang, *J. Am. Chem. Soc.*, 2010, **132**, 6498-6506.

S4 T. Lu and F. W. Chen, *J. Comp. Chem.*, **2012**, *33*, 580-592.

S5 M. J. Frisch, G. W. Trucks, H. B. Schlegel, G. E. Scuseria, M. A. Robb, J. R. Cheeseman, G. Scalmani, V. Barone, B. Mennucci, G. A. Petersson, H. Nakatsuji, M. Caricato, X. Li, H. P. Hratchian, A. F. Izmaylov, J. Bloino, G. Zheng, J. L. Sonnenberg, M. Hada, M. Ehara, K. Toyota, R. Fukuda, J. Hasegawa, M. Ishida, T. Nakajima, Y. Honda, O. Kitao, H. Nakai, T. Vreven, Jr. J. A. Montgomery, J. E. Peralta, F. Ogliaro, M. Bearpark, J. J. Heyd, E. Brothers, K. N. Kudin, V. N. Staroverov, R. Kobayashi, J. Normand, K. Raghavachari, A. Rendell, J. C. Burant, S. S. Iyengar, J. Tomasi, M. Cossi, N. Rega, J. M. Millam, M. Klene, J. E. Knox, J.B. Cross, V. Bakken, C. Adamo, J. Jaramillo, R. Gomperts, R. E. Stratmann, O. Yazyev, A. J. Austin, R. Cammi, C. Pomelli, J. Ochterski, R. L. Martin, K. Morokuma, V. G. Zakrzewski, G. A. Voth, P. Salvador, J. J. Dannenberg, S. Dapprich, A. D. Daniels, O. Farkas, J. B. Foresman, J. V. Ortiz, J. Cioslowski and D. J. Fox, Gaussian 09 (Revision E.01), Gaussian, Inc., Wallingford, CT, 2013.

S6 J. P. Perdew, K. Burke and M. Ernzerhof, *Phys. Rev. Lett.*, 1996, **77**, 3865-3868.

S7 J. P. Perdew, K. Burke and M. Ernzerhof, *Phys. Rev. Lett.*, 1997, **78**, 1396.

S8 Y. Zhao and D. Truhlar, *Theor. Chem. Acc.*, 2008, **120**, 215–241.

S9 J. D. Chai and M. Head-Gordon, *Phys. Chem. Chem. Phys.*, 2008, **10**, 6615-6620.

S10 Q. Xiao, J. Zheng, M. Li, S.-Z. Zhan, J.-H. Wang and D. Li, *Inorg. Chem.*, 2014, **53**, 11604-11615.

S11 H. V. R. Dias, H. V. K. Diyabalanage, M. G. Eldabaja, O. Elbjeirami, M. A. Rawashdeh-Omary and M. A. Omary, *J. Am. Chem. Soc.*, 2005, **127**, 7489-7501

S12 M.-K. Ehlert, S.-J. Rettig, A. Storr, R. C. Thompson and J. Trotter, *Can. J. Chem.*, 1990, **68**,

1444-1449.

S13 J. He, Y.-G. Yin, T. Wu, D. Li and X.-C. Huang, *Chem. Commun.*, 2006, 2845–2847.

S14 X.-L. Wang, J. Zheng, M. Li, S. W. Ng, S. L. F. Chan and D. Li, *Crys. Growth Des.*, 2016, **16**, 4991-4998.

S15 Y.-X. Hang, H.-R. Zhang and J. Xiang, *Z. Anorg. Allg. Chem.*, 2016, **642**, 1173-1177

S16 C. V. Hettiarachchi, M. A. Rawashdeh-Omary, D. Korir, J. Kohistani, M. Yousufuddin and H. V. R. Dias, *Inorg. Chem.*, 2013, **52**, 13576-13583

S17 J. Cored, O. Crespo, J. L. Serrano, A. Elduque and R. Giménez, *Inorg. Chem.*, 2018, **57**, 12632-12640.